




Article

Strain Pattern and Kinematics of the Canary Islands from GNSS Time Series Analysis

Jose Arnosó ^{1,2,*} , Umberto Riccardi ^{2,3} , Maite Benavent ^{2,4}, Umberto Tammaro ⁵, Fuensanta G. Montesinos ^{2,4}, Isabel Blanco-Montenegro ^{2,6} and Emilio Vélez ^{1,2} 

¹ Instituto de Geociencias (CSIC-UCM), C/Doctor Severo Ochoa 7, 28040 Madrid, Spain; emilio.velez@csic.es

² Research Group 'Geodesia', Universidad Complutense de Madrid, 28040 Madrid, Spain

³ Dipartimento di Scienze della Terra, dell'Ambiente e delle Risorse (DiSTAR), University "Federico II" of Naples, 80126 Naples, Italy; umbricca@unina.it

⁴ Facultad de Matemáticas, Universidad Complutense de Madrid, Plaza de Ciencias 3, 28040 Madrid, Spain; mbenav@ucm.es (M.B.); fuensant@ucm.es (F.G.M.)

⁵ Istituto Nazionale di Geofisica e Vulcanologia Sezione "Osservatorio Vesuviano", 80125 Naples, Italy; umberto.tammaro@ingv.it

⁶ Departamento de Física, Escuela Politécnica Superior, Universidad de Burgos, Avda. de Cantabria s/n, 09006 Burgos, Spain; iblanco@ubu.es

* Correspondence: jose.arnosó@csic.es

Received: 11 September 2020; Accepted: 5 October 2020; Published: 10 October 2020



Abstract: Following the 2004 seismic unrest at Tenerife and the 2011–2012 submarine eruption at El Hierro, the number of Global Navigation Satellite System (GNSS) observation sites in the Canary Islands (Spain) has increased, offering scientists a useful tool with which to infer the kinematics and present-day surface deformation of the Canary sector of the Atlantic Ocean. We take advantage of the common-mode component filtering technique to improve the signal-to-noise ratio of the velocities retrieved from the daily solutions of 18 permanent GNSS stations distributed in the Canaries. The analysis of GNSS time series spanning the period 2011–2017 enabled us to characterize major regions of deformation along the archipelago through the mapping of the 2D infinitesimal strain field. By applying the triangular segmentation approach to GNSS velocities, we unveil a variable kinematic behaviour within the islands. The retrieved extension pattern shows areas of maximum deformation west of Tenerife, Gran Canaria and Fuerteventura. For the submarine main seismogenic fault between Tenerife and Gran Canaria, we simulated the horizontal deformation and strain due to one of the strongest (m_{BLg} 5.2) earthquakes of the region. The seismic areas between islands, mainly offshore Tenerife and Gran Canaria, seem mainly influenced by the regional tectonic stress, not the local volcanic activity. In addition, the analysis of the maximum shear strain confirms that the regional stress field influences the E–W and NE–SW tectonic lineaments, which, in accordance with the extensional and compressional tectonic regimes identified, might favour episodes of volcanism in the Canary Islands.

Keywords: GNSS time series; kinematics and ground deformation; Canary Islands

1. Introduction

The use of permanent GNSS (Global Navigation Satellite System) stations in active geodynamic areas is increasingly gaining a pivotal role in investigating the kinematics related to tectonic plate movements, as well as crustal strain associated with tectonics, seismic cycles and/or volcanic processes (e.g., [1–4]). Presently, GNSS databases are routinely analysed by research groups and analysis centres of scientific organizations, such as the EPN (EUREF Permanent Network) from EUREF (Regional Reference Frame for Europe) or the Nevada Geodetic Laboratory [5–7]. In this study, we select an

optimal period of approximately 7 years of continuous daily GNSS solutions from the MAGNET database [6] to identify tectonic and/or geodynamic features along the Canary Islands archipelago (Spain). To improve the signal-to-noise ratio, the common-mode component [8] has been subtracted from the time series of each observation site to retrieve high-precision geodetic velocities. Then, the strain has been computed using triplets of GNSS stations in triangular elements across the entire archipelago. The study led us to obtain a reasonable description of the displacement and velocity distributions to characterize the mechanism of the current deformation in that region.

The Canary Islands is a volcanic archipelago, where space geodetic techniques, such as GNSS, might shed light on the present deformation state, which consequently is useful to manage seismic and volcanic hazards and even to improve hazard warning systems in that region. There has been limited work, by [9,10], based on GNSS data applied to study tectonics and/or crustal deformation across the Canary Islands. Ref. [9] established a GPS network that was used by different surveys and concluded that any significant deformation was not detectable throughout the archipelago due to the poor sensitivity of the geodetic network at that time. Ref. [10] used seismic data and four permanent GPS stations located on El Hierro, Tenerife, La Palma and Gran Canaria islands to depict the geodynamics and tectonic activity prior to the 2011–2012 submarine eruption at El Hierro. They detected significant surface deformation in those islands and modelled a tectonic extension between the sites in the E–W orientation from 2003 onwards. Additionally, they strongly recommended long-term monitoring of tectonic activity (seismicity and deformation) as a useful tool for the volcanic hazard assessment of future eruptive events in the Canaries. A number of papers have focused on geodynamic, tectonic and/or volcanic studies on one island of the archipelago using GNSS (e.g., [11–14]). The presence of the Teide-Pico Viejo active volcanic complex in Tenerife, for instance, makes this type of study necessary due to the enormous volcanic hazard underlying this densely populated island. The interesting papers [15,16] highlight once more the need for this kind of study. Ref. [16] reported on the deformation state of Tenerife and claimed the need for a better definition and development of CGPS (Continuous GPS) networks in that area to improve the understanding of the Tenerife kinematics and the models on rest/unrest dynamics of the Teide-Pico Viejo volcanic complex. More recently, [15] analysed GNSS data from 2005–2015, highlighting a movement of Tenerife towards Gran Canaria that is worth studying in the context of the entire Canary Islands. This would make it possible to establish whether the seismic zones between the islands affect this movement or whether it is due to the continuous slow deformation of Earth's crust.

We present a new study of the deformation pattern along the Canary archipelago through the analysis of continuous GNSS data. We use data for the 2011–2017 period to explore this active area and provide precise horizontal displacement measurements and a broad calculation of the strain, which have not been done in previous studies. With our results, we analyse the deformation obtained using the space-geodetic GNSS technique in connection with the regional tectonics, which is proven to play a key role in the volcanic eruptions that take place in the archipelago.

2. Geodynamic and Tectonic Context

The Canary Islands are an intraplate volcanic archipelago lying on oceanic lithosphere close to the Moroccan passive continental margin (Figure 1). The archipelago is located on the Nubian (African) plate, which is a very slow-moving tectonic plate. Each island forms an independent edifice, separated by narrow channels, except for Lanzarote and Fuerteventura, which share a NNE-trending submarine ridge parallel to the African coast (e.g., [17–19]). Each island in the Canary archipelago thus has an independent history and starting activity at different times and is evolving differently, making it difficult to establish a general evolutionary model [20–22]. Although the eastern islands (Lanzarote, Fuerteventura and Gran Canaria) are in a post-erosional stage of growth, the western islands (Tenerife, La Gomera, La Palma and El Hierro) are in a shield stage of growth, although La Gomera, which is a volcanic edifice with a complex and extensive evolution and a mid-level erosional stage, represents a post-shield gap [23].

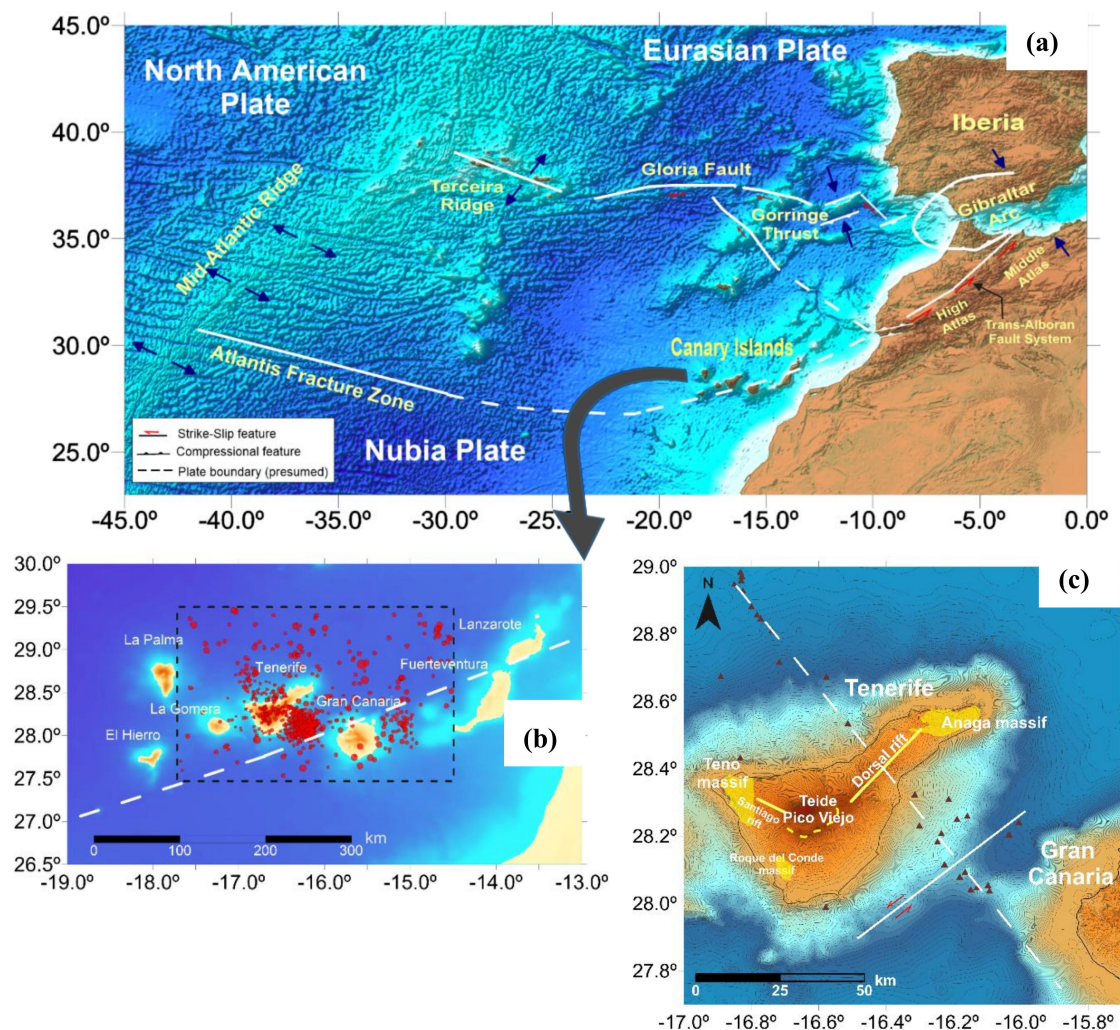


Figure 1. (a) Digital elevation map of the central Atlantic area near the Canary Islands based on the GEBCO (General Bathymetric Chart of the Oceans) dataset (<https://www.gebco.net>). The main tectonic features and regimes are indicated along the plate boundaries. (b) Map showing the seven major islands of the Canary Archipelago and the epicentres of the earthquakes (mbLG > 1.2) recorded in the dashed rectangular area during 2011–2017. The white dashed line that crosses the archipelago marks the presumed southern boundary of the Morocco microplate, as proposed by [24]. (c) Some geological features of Tenerife: rifts (solid yellow lines); massifs (yellow areas); the Teide-Pico Viejo volcanic complex; the Las Cañadas caldera wall (dashed yellow line); the volcano-tectonic direction (dashed white line), which is an inferred submarine alignment based on the volcanic seamount distribution (brown triangles) and a slope break in the SW flank of Gran Canaria proposed by [25]; and the sinistral strike-slip fault (solid white line) located between Tenerife and Gran Canaria.

The origin of the Canary Islands is still controversial: a mantle plume, regional tectonics or a combination of both are still under debate, although the unifying model of [26] is the most accepted model. Several authors (e.g., [26–28]) have proposed a link between the Atlas Mountains in Africa and the genesis of the Canaries based on magmatism and tectonic analogies. Ref. [26] hypothesized the existence of a residual plume under North Africa, the Canary Islands and the Western Mediterranean and a fracture system that allows the magma to ascend. Recent geodynamical models propose intraplate tectonics driven by asthenospheric upwelling (mantle plumes), while others are based on plate boundary processes or lithospheric thinning that favour asthenospheric upwelling [29,30]. Ref. [10] showed that anomalous tectonic activity at different spatiotemporal scales in the Canary

Islands region since 2003 preceded the El Hierro magmatic activity that gave rise to the recent submarine eruption in 2011. In addition, [31] emphasized that there is no conflict between the mantle flow model and the involvement of lithospheric processes in magma generation and ascent in the Canary Islands. Additionally, they aimed to determine the distribution of volcanism through the interaction among the delamination of subcontinental lithospheric mantle material, inflow of mantle plume material and reactivation of geological structures driven by the African–European convergence.

The Eurasia–Africa kinematics, the Mid-Atlantic Ridge and other regional structures control the plate-scale stress field in the Canary archipelago [32]. Likewise, the regional fault systems influence the tectonics in the region. In particular, [24] suggested the connection between the fault systems related to the Mid-Atlantic Ridge (NE–SW orientation) and the Trans-Alboran Fault System (NE–SW orientation), which runs along the Atlas Mountain range (northwestern Africa), to explain the kinematics of the Africa–Eurasia plate. These authors proposed that the Moroccan microplate passed through the Canary archipelago at its southern limit, limiting the extension of the Trans-Alboran Fault System to the Atlantis Fracture Zone (see Figure 1). The Moroccan microplate is decoupled from the Eurasian plate by tectonic activity in the Gibraltar–Azores belt, the Gorringe thrust, the Gloria fault and the Terceira ridge. The strike-slip motion at the Canary–Transalboran fault system results in decoupling from the Nubian plate, and the boundary between Moroccan microplate and North American plate undergoes an E–W stretching [24]. A submarine sinistral strike-slip fault, with reverse components, is located between Tenerife and Gran Canaria, and its motion results in the underthrusting of the western block (Tenerife) and a southwest relative displacement of Tenerife with respect to Gran Canaria and Africa (Figure 1). Refs. [28,33] proposed the existence of this crustal fracture based on seismic and gravity data analysis. In addition, [34] studied the focal mechanism of the Mw 4.0 earthquake preceding the 2011 eruption at El Hierro. They found NNW–SSE horizontal compression and E–W quasi-horizontal extension, suggesting that the rupture process was related to tectonic stress. In addition, [35], after analysing the seismicity that occurred at El Hierro during 2011–2014, proposed that the movement of a regional fault triggered the 2011 eruption and speculated that local tectonics, not magma overpressure, facilitated magma ascent. The NNW–SSE orientation matches the orientation of stresses obtained by [33] using data from the moderate Mw 5.0 earthquake that occurred between Tenerife and Gran Canaria in 1989 and agrees with the orientation of the regional compression model described by [36,37] for the archipelago. Recent aeromagnetic studies by [38–40] in the central islands of the archipelago revealed elongated anomalies with E–W (Tenerife and La Gomera) and ENE–WSW (Gran Canaria) orientations. Furthermore, [39] accounted for the intrusive body found in the submarine edifice of Gran Canaria, which has an ENE–WSW orientation that coincides with the aforementioned fracture suggested by [28]. All these facts shed light on the role of regional tectonics in the origin of the Canary Islands and the magma upwelling from the mantle.

3. Analysis of GNSS Data

GNSS-derived strain rates have countless applications in geosciences, including, for instance, in seismotectonic and geodynamic studies aimed at comparing stress fields and rates to explain earthquake occurrence or interpret peculiar plate motion features in diffuse plate boundary areas [41]. Currently, there are two possible approaches to estimate strains from GNSS observations. A gridded approach, called least-squares collocation (LSC), consists of inverting a uniform velocity field to the strain rate field [42,43] or calculating strain rates in triangular or more complex segments [44]. A very detailed description of the pros and cons of the different methods of strain retrieval can be found in [45]. Briefly, in the LSC method, the velocities of n stations obtained in t_1 and t_2 GNSS survey campaigns or in a time interval $T = t_2 - t_1$ from permanent stations are used to reconstruct a continuous velocity field. However, to move from a discrete collection of measurements in time/space to a continuous field, a generalized interpolation problem must be solved. Ref. [45] found that the strain rate field obtained in such a way leads to clearer deformation patterns than that retrieved from the discrete triangle or "segmentation" method. Although many recent works (e.g., [46–48]) are still based on the

segment (triangular) approach, the main motivation for this choice is that it allows avoidance of any distortion of the GNSS network caused by the datum itself. Moreover, this method has proven to be more suitable for not only highlighting discontinuities of the strain field, such as faults, which make the strain field highly nonuniform, but also strain analysis over small areas with a limited number of measurement points. This is why geodesists still use similar methods for local strain analysis related to, for instance, mine exploitation or volcano monitoring [47,49]. For these reasons, we decide to use the same approach. With this method, the area is segmented into several geometrical units, the local strain and rotation rates are computed for each unit, and finally, all the individual results are integrated. Although the segmentation method, in principle, is not exclusively limited to triangulation (it can have any geometrical shape), Delaunay triangulation of the measurement points remains the most used for this approach.

The analysed GNSS data set comprises a time series of 3D (North, East, Up) site positions, which are available as daily solutions produced by the Nevada Geodetic Laboratory [6]. The solid earth and pole tide contributions are reduced according to the “IERS 2010 Conventions” [50], while ocean tide loading (diurnal, semidiurnal, Mf and Mm waves) accounts for FES2004 [51]. The data set encompasses 6.7 years between 2011 and 2017 and refers to GNSS sites spanning the Canary archipelago (Table 1, Figure 2). The daily GNSS solutions refer to the IGS14 realization of the International Terrestrial Reference Frame 2014 (ITRF2014) [52].

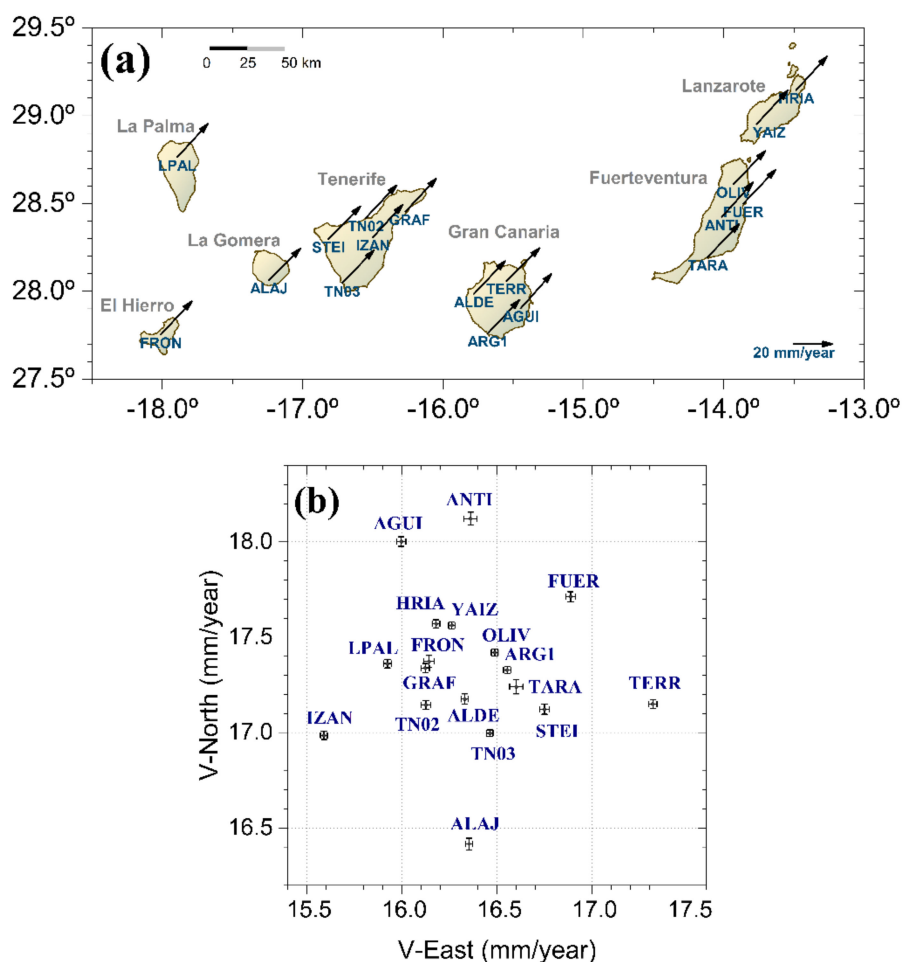


Figure 2. (a) Global Navigation Satellite System (GNSS) station velocities for April 2011 to December 2017 with respect to the ITRF2014 frame. (b) Velocity space calculated after the common-mode component (CMC) analysis. The error bars centred at each station indicate one-sigma uncertainty.

Table 1. Geographic coordinates of the GNSS stations employed in this study. Horizontal velocities (V_x , V_y) and standard deviations (SD_{V_x} , SD_{V_y}) after filtering out the common-mode bias. Velocity and standard deviation units are mm/year.

Station	Island	Longitude (°)	Latitude (°)	Height (m)	V_x	SD_{V_x}	V_y	SD_{V_y}
FRON	El Hierro	−18.011	27.754	308.2	16.1	0.03	17.4	0.03
LPAL	La Palma	−17.894	28.764	2199.2	16.0	0.02	17.9	0.03
ALAJ	La Gomera	−17.241	28.064	899.1	16.6	0.02	16.9	0.03
TN02	Tenerife	−16.551	28.418	54.5	16.1	0.03	17.2	0.02
TN03	Tenerife	−16.719	28.047	58.5	16.5	0.02	17.0	0.02
IZAN	Tenerife	−16.500	28.308	2417.5	16.0	0.02	17.0	0.02
STEI	Tenerife	−16.816	28.298	988.6	16.8	0.02	17.1	0.03
GRAF	Tenerife	−16.268	28.454	138.5	16.1	0.02	17.3	0.02
ALDE	Gran Canaria	−15.780	27.985	122.4	16.3	0.02	17.2	0.03
ARG1	Gran Canaria	−15.681	27.761	67.8	16.5	0.02	17.4	0.02
AGUI	Gran Canaria	−15.446	27.904	329.1	16.0	0.02	18.0	0.03
TERR	Gran Canaria	−15.548	28.060	648.8	17.3	0.02	17.2	0.02
OLIV	Fuerteventura	−13.928	28.610	275.0	16.6	0.02	17.3	0.02
FUER	Fuerteventura	−13.860	28.499	76.8	16.9	0.03	17.7	0.03
ANTI	Fuerteventura	−14.014	28.423	316.0	16.4	0.03	18.1	0.03
TARA	Fuerteventura	−14.115	28.194	60.0	16.6	0.04	17.2	0.04
HRIA	Lanzarote	−13.485	29.145	319.8	16.2	0.02	17.6	0.02
YAIZ	Lanzarote	−13.766	28.952	233.5	16.3	0.02	17.7	0.02

It is common knowledge that antenna motion, not ground displacement, is directly observed; thus, to observe crustal movements, all site self-motions should be eventually excluded so that the observed displacement of antennas could be interpreted as a real tectonic motion. This is mainly true in regions where crustal deformations are small; consequently, noise in calculated geodetic strain rates, which in general are smaller and less reliable, could be considerable and even larger than the tectonic signal.

Therefore, in our analysis, after removing outliers due to nearby earthquakes and known equipment changes from the GNSS time series, the signal-to-noise ratio in the daily solutions is improved by using the common-mode error according to the formulation proposed by [8]. This method is a stacking technique resulting in spatial filtering aimed at removing random noise and extracting spatially correlated transients, the so-called common-mode component (CMC), that deviates from a zero mean over the span of the position time series of a continuous GNSS network. A well-known kind of CMC in continuous GNSS position time series, especially in the vertical direction, is the seasonal motion, with mostly annual and semi-annual periodicities. Such an approach [8] consists of a three-step procedure:

- (1) Residuals-Stacking-Filtering: for each daily solution (d) and GNSS site (s), the residual (r) [observed (O)-predicted value (C)] is computed:

$$r_s(d) = O^s(d) - C^s(d) \quad (1)$$

- (2) Computation of the common mode by means of stacking, by averaging the residuals from all the sites (S) in the network:

$$r(d) = \frac{\sum_{s=1}^S r_s(d)}{S} \quad (2)$$

Equation (2) represents the common-mode bias, which, in principle, should improve with the number of sites.

- (3) Filtering: for each site, the common-mode bias is subtracted from the observed position, resulting in a filtered position:

$$\hat{O}_s(d) = O^s(d) - r(d) \quad (3)$$

Thanks to this filtering, we are hopefully able to remove any signal common to a subset of GNSS stations from position time series, regardless of the origin.

As a result, we obtain a lower standard error on the retrieved linear trend (ITRF absolute velocity).

For such improved velocities (Table 1), we compute, for each geometrical unit (triangle), the bi-dimensional horizontal infinitesimal strain from 23 sets of three non-co-linear GNSS stations each, forming triangles, as formulated by [53] for a flat earth.

Under the assumption that the partial derivatives of the displacement, denoted in vector notation by u of components (u_x, u_y) are small, several approximations can be made in the calculations, which lead to the following results about the normal strains corresponding to the x and y directions at point (x, y) :

$$\varepsilon_{xx} = \frac{\partial u_x}{\partial x} \quad \varepsilon_{yy} = \frac{\partial u_y}{\partial y} \quad (4)$$

Customarily, negative values of ε indicate contraction, while positive values represent stretching. In addition to stretching and contraction, the change in the angle between the positions before and after deformation is known as the shear strain. In particular, the shear strain ε_{xy} is defined as half the increase in the angle formed by two infinitesimal line segments that initially are parallel to the x and y axes.

$$\varepsilon_{xy} = \frac{1}{2} \left(\frac{\partial u_x}{\partial y} + \frac{\partial u_y}{\partial x} \right) \quad (5)$$

Following this definition and considering symmetry, $\varepsilon_{yx} = \varepsilon_{xy}$. These components are the four elements of the strain matrix.

$$\epsilon = \begin{bmatrix} \varepsilon_{xx} & \varepsilon_{xy} \\ \varepsilon_{yx} & \varepsilon_{yy} \end{bmatrix} \quad (6)$$

Therefore, as discussed above, the strain is a function of the normal strains, shear strains and rotation (Θ).

$$\epsilon = f(\varepsilon_{xx}, \varepsilon_{yy}, \varepsilon_{xy}, \Theta) \quad (7)$$

$$\Theta = \frac{1}{2} \left[\arctg \left(\frac{\varepsilon_{xy}}{\varepsilon_{yy} - \varepsilon_{xx}} \right) \right] \quad (8)$$

$$\varepsilon_i = \varepsilon_{yy} * \cos^2 \Theta_i + \varepsilon_{xx} * \sin^2 \Theta_i + \varepsilon_{xy} * \sin \Theta_i * \cos \Theta_i \quad (9)$$

By setting $i = 1, 2$, ε_1 and ε_2 become the two principal horizontal strains, and the maximum shear strain is

$$\frac{1}{2} (\varepsilon_1 - \varepsilon_2) \quad (10)$$

In our analysis, the following first-order assumptions are implicitly made:

- (1) As the study area is small, the sphericity of Earth is neglected, and the Earth's surface is approximated by a flat surface model. Hence, plane-strain deformation remains in the horizontal plane.
- (2) Considering the principles of mechanics, we assume that the deformation of networks reflects the real movements of Earth's crust and that the area between geodetic points could be considered as a continuous medium in which the strain is homogeneously distributed across the triangular area between the three GNSS sites.
- (3) Vertical velocities do not significantly affect the physical interpretation of the strain. Even if the latter assumption above is naive in areas displaying significant uplift or subsidence, in our case, stations with negligible vertical displacement (<3 mm/year) have been selected; hence, we are confident that 2D strain can provide useful insights into ground deformation patterns. The parameters of the strain were calculated from displacements (u_x, u_y) estimated by a constant velocity for the whole study period (6.7 years between 2011 and 2017). The velocities measured at the three GNSS sites are the result of the three components of crustal velocity: translation, rotation

and distortion. For each of the GNSS sites, we know the horizontal coordinates of the initial site location (x_0, y_0) as well as the east–west and north–south instantaneous velocities (V_x, V_y) . We solve for the “3-site triangle strain” problem, which is a well-known perfectly constrained problem [43] (p. 157). The principal strain axes are found by computing the eigenvectors of the 2-D strain tensor ϵ . The eigenvectors are unit vectors in the directions of the principal strain axes. The eigenvalues of ϵ are the principal extensions in the principal directions. The larger of the two eigenvalues are the greater principal extension, ϵ_1 , and the length of the semi-major axis of the horizontal strain ellipse is equal to the greater principal strain, $S_1 = \epsilon_1 + 1$. The semi-minor axis is $S_2 = \epsilon_2 + 1$, where ϵ_2 is the lesser principal extension. For each triangle, we compute the strain in terms of elongations (strain unit) and resulting dilatation (mean strain), the latter of which is referred to as the triangle centroid. The main strain parameters for each triangle are listed in Table 2. Included in the Supplementary Materials is Figure S1, which illustrates the geometric configuration of each triangle.

Table 2. Strain parameters calculated for each triplet of GNSS stations: elongation, shortening, principal strains ϵ_1, ϵ_2 and their respective principal directions θ_1, θ_2 , and dilatation. The strain and elongation/shortening units are 10^{-9} .

	Triangles	Baseline	Elongation/ Shortening	ϵ_1	θ_1 (°)	ϵ_2	θ_2 (°)	Dilatation
1	ALDE-GRAF-TN03	ALDE-GRAF ALDE-TN03 GRAF-TN03	24.92 −10.53 −0.79	37.49	−13.0	−15.54	77.0	21.96
2	ALDE-HRIA-TN03	ALDE-HRIA ALDE-TN03 HRIA-TN03	1.89 −10.53 −1.15	6.46	32.7	−15.27	−57.3	−8.81
3	ALDE-OLIV-TN03	ALDE-OLIV ALDE-TN03 OLIV-TN03	9.28 −10.53 3.92	15.21	48.8	−34.46	−41.2	−19.24
4	ALDE-LPAL-YAIZ	ALDE-LPAL ALDE-YAIZ LPAL-YAIZ	13.60 3.94 5.80	23.31	−21.8	3.66	68.2	26.97
5	HRIA-LPAL-YAIZ	HRIA-LPAL HRIA-YAIZ LPAL-YAIZ	4.27 −11.54 5.80	19.01	−53.0	−13.48	37.0	5.53
6	ALDE-OLIV-YAIZ	ALDE-OLIV ALDE-YAIZ OLIV-YAIZ	9.28 3.94 17.42	78.95	−40.2	0.77	49.8	79.72
7	GRAF-OLIV-YAIZ	GRAF-OLIV GRAF-YAIZ OLIV-YAIZ	12.64 5.06 17.42	63.56	−33.7	−3.57	56.3	59.99
8	LPAL-OLIV-YAIZ	LPAL-OLIV LPAL-YAIZ OLIV-YAIZ	10.97 5.80 17.42	55.97	−29.3	−6.90	60.7	49.08
9	LPAL-TN03-ALAJ	LPAL-TN03 LPAL-ALAJ TN03-ALAJ	31.34 73.84 −0.28	162.36	8.9	−2.02	−81.1	160.34
10	GRAF-LPAL-ALAJ	GRAF-LPAL GRAF-ALAJ LPAL-ALAJ	8.36 6.70 73.84	104.85	−5.9	−3.19	84.1	101.65
11	ALDE-LPAL-ALAJ	ALDE-LPAL ALDE-ALAJ LPAL-ALAJ	13.60 −7.41 73.84	122.68	−0.7	−8.35	89.3	114.33

Table 2. Cont.

	Triangles	Baseline	Elongation/ Shortening	ϵ_1	θ_1 (°)	ϵ_2	θ_2 (°)	Dilatation
12	ALDE-GRAF-ALAJ	ALDE-GRAF ALDE-ALAJ GRAF-ALAJ	24.92 −7.41 6.70	59.53	3.8	−7.41	−86.2	52.12
13	LPAL-ALAJ-FRON	LPAL-ALAJ LPAL-FRON ALAJ-FRON	73.84 2.44 −4.59	103.20	−7.5	−8.77	82.5	94.43
14	LPAL-FRON-STEI	LPAL-FRON LPAL-STEI FRON-STEI	2.44 48.44 −8.96	94.00	−31.3	−73.39	58.7	20.61
15	ALAJ-FRON-ARG1	ALAJ-FRON ALAJ-ARG1 FRON-ARG1	−4.59 −7.88 −6.43	−4.41	−84.6	−201.55	5.4	−205.96
16	FRON-IZAN-ARG1	FRON-IZAN FRON-ARG1 IZAN-ARG1	7.53 −6.43 29.90	30.32	−56.0	−84.65	34.0	−54.33
17	ALAJ-IZAN-ARG1	ALAJ-IZAN ALAJ-ARG1 IZAN-ARG1	−50.71 −7.88 29.90	43.75	−30.4	−54.23	59.6	−10.48
18	TN03-ALAJ-STEI	TN03-ALAJ TN03-STEI ALAJ-STEI	−0.28 6.92 91.42	116.91	36.1	−50.02	−53.9	66.89
19	IZAN-ARG1-TERR	IZAN-ARG1 IZAN-TERR ARG1-TERR	29.90 111.30 10.95	169.18	77.1	−65.34	−12.9	103.84
20	GRAF-TERR-ANTI	GRAF-TERR GRAF-ANTI TERR-ANTI	89.95 6.88 −29.10	117.47	−33.6	−45.58	56.4	71.89
21	STEI-TN03-GRAF	STEI-TN03 STEI-GRAF TN03-GRAF	6.92 −64.43 −0.79	40.92	11.7	−96.23	−78.3	−55.31
22	STEI-TN03-IZAN	STEI-TN03 STEI-IZAN TN03-IZAN	6.92 −252.90 −100.90	22.20	−4.6	−253.76	85.4	−231.56
23	TN02-IZAN-GRAF	IZAN-GRAF IZAN-TN02 GRAF-TN02	153.00 −23.81 4.87	202.06	33.0	−138.42	−57.0	63.64

4. Results

Figure 2 displays the velocities (horizontal component) and the velocity space calculated after the CMC analysis with respect to the ITRF2014 frame for all GNSS stations used in this study. The retrieved velocity field is relatively dense compared to the individual size of each island. The velocities are mostly grouped, except for three sites around the central islands (IZAN, TERR, ALAJ in Tenerife, Gran Canaria and La Gomera, respectively). For all the sites, the mean value of the velocity module is 23.8 ± 0.38 mm/year with an azimuth of $46.7 \pm 0.95^\circ$ E, which agrees with the Nubia plate velocity from the NUVEL-1A model [54]. This is in accordance with the mean value of approximately 23.2 ± 1.03 mm/year in the NNE direction calculated by [9] for three permanent stations located on Lanzarote, Gran Canaria and La Palma during 2002–2009.

The horizontal displacements were estimated from the improved velocities after CMC filtering (see Section 3), which were considered constant for the time interval of 6.7 years used in this study. Then, to interpret the crustal motions along the Canary archipelago, we computed the strain parameters for each triplet of GNSS stations following the segmentation (triangle) method. Table 2 lists all the numerical results in terms of baseline length and triangle area change. To facilitate the reading of the

results obtained on the triangular mesh network covering the entire archipelago, the largest elongation and shortening values are collected in Table 3. These should reportedly reflect the main tectonic changes unveiled by our strain analysis. The pattern that emerges from this analysis clearly shows that the baselines encompassing the known fault line intersecting Tenerife and Gran Canaria undergo the maximum elongations (Figure 3).

Table 3. Summary of the main tectonic changes as derived from the strain analysis. The elongation/shortening units are 10^{-9} .

Baseline	Largest Elongation	Baseline	Largest Shortening
LPAL-ALAJ	73.84	ALDE-TN03	-10.53
LPAL-TN03	31.34	TN03-IZAN	-100.90
ALDE-GRAF	24.92	STEI-GRAF	-64.43
IZAN-TERR	111.30	STEI-IZAN	-252.90
IZAN-GRAF	153.00	IZAN-TN02	-23.81
		TERR-ANTI	-29.10
		HRIA-YAIZ	-11.54

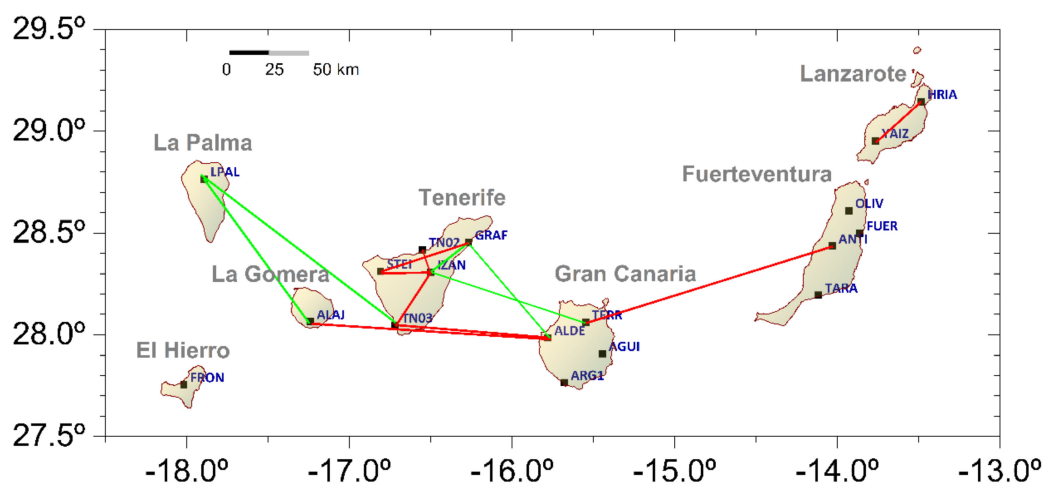


Figure 3. Baselines with the maximum variation in length during the period of observation (2011 to 2017). The green lines indicate the greatest elongation ($\geq 10^{-8}$), and the red lines indicate the greatest shortening ($\geq 10^{-8}$).

The elongations between northeast Tenerife (IZAN and GRAF sites) and northwest Gran Canaria (TERR and ALDE sites) are on the order of 10^{-8} , and the baseline IZAN-TERR undergoes the largest elongation in this zone (1.113×10^{-7}). In addition, the baselines connecting the island of La Palma with Tenerife and La Gomera (LPAL-TN03 and LPAL-ALAJ, respectively) also exhibit relevant elongations on the order of 10^{-8} . Large baseline shortenings are encountered for the central islands of the archipelago. Figure 3 gathers and displays the shortening values of approximately 10^{-8} , where the baseline stands out between southwest Tenerife (TN03) and west Gran Canaria (ALDE). The baselines connecting west Gran Canaria (ALDE) with La Gomera (ALAJ) and northeast Gran Canaria (TERR) with the central part of Fuerteventura (ANTI) are also remarkably contracted for the same order of magnitude. In accordance with those results, [9], using episodic GPS observations, reported length variations of approximately 9 to 10 mm for the respective baselines between Gran Canaria and La Gomera and between La Palma and Fuerteventura during 2003–2005. Likewise, the same authors reported length variations of approximately 7 to 8 mm for the respective baselines between La Palma and Fuerteventura and between Gran Canaria and Fuerteventura during 2003–2009. Considering the distance between GPS sites, all these values represent variations of approximately 10^{-8} .

It is worth noting the particular case of Tenerife. The mean velocity computed from five GNSS stations (Table 1) is 23.6 ± 0.3 mm/year, which is in agreement with the value reported by [16], 23.3 ± 0.2 mm/year, determined by analysing daily GNSS solutions of four sites distributed across the island for the period 2008–2015. This value is also close to the velocity estimated by [15], 23.1 ± 0.5 mm/year, using a set of nine GNSS stations between 2005 and 2015.

Regarding Lanzarote, we found that the baseline YAIZ-HRIA has a remarkable shortening of approximately 10^{-8} . This is consistent with a recent detailed geodetic study by [14] of the Timanfaya volcanic area. The authors, relying on three years (2014–2017) of continuous GNSS data and approximately twenty years (1997 to 2017) of continuous tilt and strain measurements, detected a subsidence and a peculiar behaviour in the southwest sector of Lanzarote. This result is also in agreement with that achieved by [55] using InSAR data pointing to 6–7 mm/year subsidence in the Timanfaya volcanic area. Other baselines along the archipelago show negligible elongations or shortenings on the order of 10^{-9} (Table 2).

5. Discussion

Considering the baseline calculations listed in Tables 2 and 3, the most relevant changes on the order of 10^{-7} are encountered on Tenerife. The largest elongation occurs along the baseline IZAN-GRAF (1.530×10^{-7}), and the largest shortenings occur along the baselines STEI-IZAN (-2.529×10^{-7}) and TN03-IZAN (-1.009×10^{-7}). This indicates a differential kinematic behaviour of the central and western areas with regard to the northeast Tenerife. Indeed, the northeast area comprises the stable sector of the Anaga massif, which is a portion of the old basaltic shield structure of the island together with the Teno and Roque del Conde massifs [56], and part of the Dorsal Rift fissure system (see Figure 1). Ref. [16] retrieved different deformation patterns for Tenerife, such as compression in the central-western part and extension to the northeast part (parallel to the Dorsal rift). Likewise, [15] pointed out the subdivision of Tenerife into two areas with different kinematic behaviours: extension in the northeast and central areas of the island and compression in the west. According to these authors, the different behaviours observed in the two deformation patterns along the island could be produced by the effect of the submarine fault (Figure 1). Ref. [57] described the large-scale deformation pattern found along Tenerife as due to predominant vertical kinematics and proposed gravitational sinking of the island's edifice as a mechanism. Later, [16] even reported a decrease in elevation, although they explained the observed subsidence by the combined effect of the lateral spreading of the elastic lithosphere and the descent of the water table level in the island. To understand these findings within the general framework of tectonics of the entire archipelago, our result suggests that the behaviour of the northeast sector of Tenerife follows the predominant extensional regime in the archipelago (see Figures 4 and 5) and could be a consequence of the effects of the submarine fault in the tectonic regime in this area.

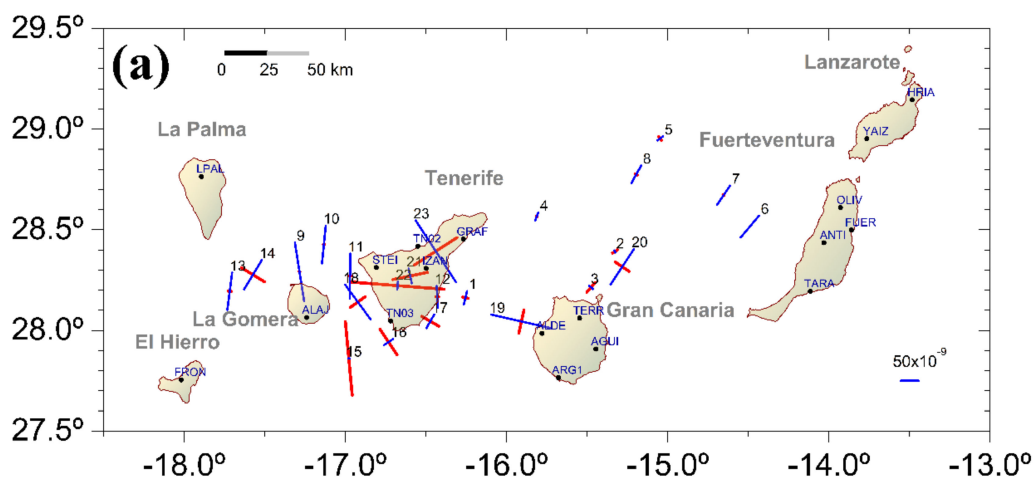


Figure 4. Cont.

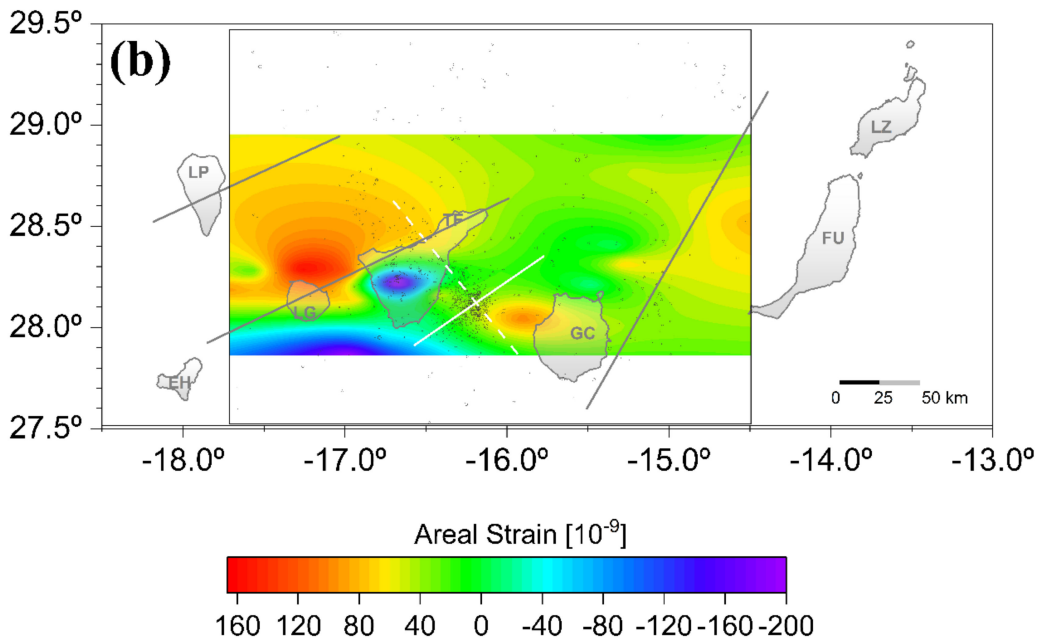


Figure 4. (a) Strain centroids determined by the principal axes of the 2D strain tensor calculated for 23 triangles established among the GNSS stations used in this study. Blue and red colours show tensile and compressive strain, respectively. (b) Contour map showing the areal strain distribution according to the colour bar. The thick white line represents the major fracture (submarine reverse fault between Gran Canaria and Tenerife), and the dashed white line is the secondary fault (inferred submarine alignment and slope break). The solid grey lines indicate other important volcano–tectonic features of the Canarian Archipelago (e.g., [28,33]). The grey circles are the epicentres of the earthquakes ($m_{bLG} > 1.2$) recorded in the rectangular area during the period 2011–2017. EH: El Hierro; LP: La Palma; LG: La Gomera; TF: Tenerife; GC: Gran Canaria; FU: Fuerteventura; LZ: Lanzarote.

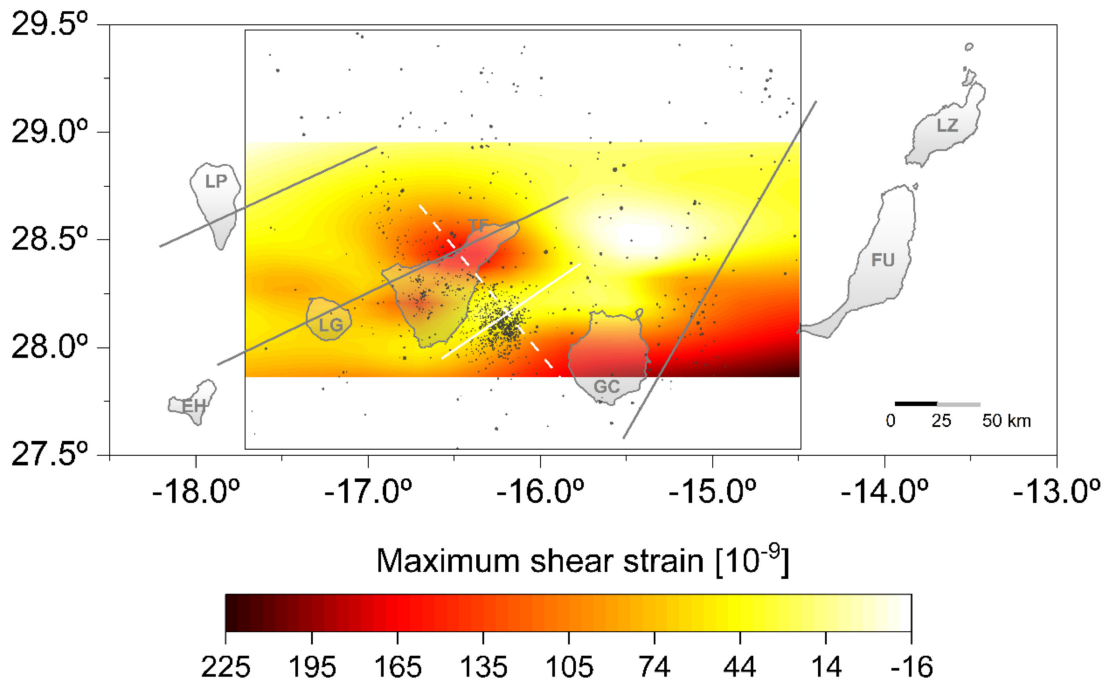


Figure 5. Same contour map as Figure 4b but for maximum shear strain.

Figure 4a shows the horizontal strain centroids determined from the principal axes of the 2D strain tensor calculated for the 23 triangles (see Table 2) defined by the GNSS stations. On the one hand, the magnitude of the tensile strains ranges from -4×10^{-9} to 203×10^{-9} , and that of the compressive strains from -254×10^{-9} to 4×10^{-9} (respectively, blue and red colour in Figure 4a). The general pattern of the principal strain axes reveals that the largest magnitudes are localized around the central islands of the archipelago. There are significant changes in the strain orientation pattern as well. The extension (tensile strain) of the eastern islands is generally trending NE, whereas that of the central and western islands is trending NNW. There is evidence of a wide area of crustal compression around the central and western sectors of Tenerife, from a dominant WNW direction. This finding is in accordance with the stress field modelling of [32] for the Canary Islands, which indicates that the stress distribution and orientation vary considerably after the Atlantis Fracture Zone is included (Figure 1), enabling the detection of areas of extension and strike-slip and not just a compressive regime through the whole archipelago. Table 4 lists the largest elongation and contraction values found in this triangle strain analysis. On the other hand, the strain tensor calculation allows us to draw a dilatation map of the archipelago, which gives us an idea of the areas of horizontal strain accumulation that might be related to surface deformation produced by tectonic stress or fault activity. Thus, the negative values in Figure 4b indicate compression, and the positive values indicate extension. The figure also shows the seismic activity recorded by the National Geographic Institute (IGN) of Spain localized in the surroundings of the central islands of the archipelago for the period of study (2011–2017). A clear extension pattern along the archipelago might be identified, and the areas of maximum deformation are located to the west of Tenerife, Gran Canaria and Fuerteventura. Additionally, the distribution of areal strain results in the predominant tensile behaviour in terms of the principal strain above the major fracture between Tenerife and Gran Canaria. This is in agreement with the extension in the E–W direction since 2003, as suggested by [10] after analysing GPS data from two stations situated on La Palma and Gran Canaria.

Table 4. Main tectonic change, as derived from the strain analysis, expressed as dilatation or contraction of the triangles (triangle numbers as in Table 2). Units are 10^{-9} .

	Triangle	Largest Dilatation		Triangle	Largest Contraction
9	LPAL-TN03-ALAJ	160.34	3	ALDE-OLIV-TN03	−19.24
10	GRAF-LPAL-ALAJ	101.65	21	STEI-TN03-GRAF	−55.31
11	ALDE-LPAL-ALAJ	114.33	22	STEI-TN03-IZAN	−231.56

Generally, areas undergoing compression in the archipelago overlap the location of most of the epicentres during this period of study. Most of the seismicity is concentrated in the area between Tenerife and Gran Canaria (Figure 4b). Moderate-to-large ($M_w > 6.0$) tectonic earthquakes are likely to occur due to the presence of the northeast–southwest trending submarine fault, which is the main tectonic feature of the archipelago [58]. Compression occurs in the central area of Tenerife and to the south of La Gomera and Tenerife. In fact, there is a considerable change in the strain pattern along Tenerife, where maximum compression appears in central Tenerife and moderate extension occurs to the northeast, which is a clear consequence of areas with differential kinematics.

The aforementioned local shortening should cause compression in central Tenerife and may correspond to the ground subsidence in the Teide volcanic edifice. Indeed, the 2004–2005 seismic crisis of Teide (e.g., [59]) was a consequence of magma injection in the northwestern rift of Tenerife that later produced a fluid pressure increase during magma migration and was responsible for the gravity increase detected by [60]. As [15] pointed out, a decrease or stabilization of pressure after such a fluid migration might trigger compressional processes in the central area of Tenerife. However, our analysis spans the years 2011–2017, years after that seismic crisis, and the seismicity (see Figure 1) and monitoring techniques during that period did not show other symptoms of Teide volcano reawakening. In addition, previous studies based on GNSS and InSAR that cover different

periods after the 2004 seismic crisis in Tenerife (e.g., [15,16,57]) all refer to subsidence in the central area of the island. The change from the dilation to compression pattern, from north to south along La Gomera Island, exhibits a well-defined E–W orientation. This is consistent with the regional fractures in the strike-slip tectonic regime suggested by [28] and later supported by other authors [10,32,33,61]. More recently, refs. [39,40] suggested that such an orientation could be responsible for the ascent and emplacement of magmas in the early formation phases of the central islands of the archipelago. Moreover, such a deformation pattern with an east–west orientation in the central islands is consistent with the existence of the major tectonic feature that connects the Trans-Alboran Fault System with the Mid-Atlantic Ridge, as suggested by [24] (see Figure 1).

To deepen into the spatial distribution of the seismicity, we compute and map the magnitude of the 2D maximum shear strain for most of the archipelago (Figure 5). An abrupt change in shear strain (of approximately 100×10^{-9}) clearly appears between Tenerife and Gran Canaria along the NE–SW trending fault. This is an important seismogenic area where a submarine reverse fault separates two insular blocks [33]. This area, during the period of observation, was affected by a cluster of earthquake epicentres, ranging from low to moderate magnitude (from m_{bLG} 1.2 to m_{bLG} 3.4).

We used Coulomb software (release 3.4) [62,63] to simulate the horizontal deformation and strain caused by the 1989 m_{bLG} 5.2 earthquake that occurred offshore between Tenerife and Gran Canaria at a focal depth of approximately 15 km. The study of the focal mechanism of the main shock by [33] reported a sinistral strike-slip fault oriented NE–SW, matching the strike of the aforementioned submarine fault [28]. According to Okada's formulae [64], Coulomb 3.4 calculates the 3D component of the displacement field due to a finite rectangular source dislocation buried in an elastic half-space. This formulation approximates the surface movements produced by earthquake faulting, making it appropriate for modelling crustal deformation measured by geodetic techniques. Dilatation is computed from components $\varepsilon_1 + \varepsilon_2 + \varepsilon_3$; that is, by summing the normal strains in the three directions (X, Y, Z), supposing a 3D representation. In our computation, we used the 2D plane strain approximation. Figure 6 maps the dilatation and maximum shear strain (Equation (10)) produced by a rectangular source whose top and bottom range from the surface down to 15 km. The calculation depth is fixed at 4 km b.s.l., but in our simulation, we tested different depths (up to 0 km, seafloor) and observed negligible differences, so Z is constant in the resulting map. Okada's source is embedded in an elastic half-space homogeneously parametrized as having a given Young's modulus ($E = 80$ GPa), typical of oceanic crust, and Poisson's ratio ($\sigma = 0.25$). Table 5 lists the values of the main parameters used in our computation. The resulting fields of both dilatation and maximum shear strain are in good agreement with the triangle strain fields (compare Figure 6a and Figure 4b, Figure 6b and Figure 5). The negative values of maximum shear strain (Figure 6b), which accordingly indicate a sinistral strike-slip, define a patch of the field oriented towards Gran Canaria, trending in the NW–SE direction, similar to the result of the GNSS triangle strain (Figure 5) that shows two maximum shear strain highs located to the North of Tenerife and to the West of Gran Canaria. This demonstrates that earthquakes cause static stress changes within the lithosphere able to trigger measurable transient deformation of the Earth's surface. GNSS can sense both the spatial and temporal characteristics of pre- and post-seismic deformation. In the far field, geodetic data have been used to characterize both coseismic deformation and viscoelastic relaxation following large strike-slip earthquakes [65], i.e., the long-term seismic cycle. This is often called the stick-slip behaviour of a fault. During the earthquake, the elastic strain built-up in the surrounding crust during the interseismic interval is transformed into permanent slip. Deformation following a large earthquake can continue aseismically for months or even years in the form of viscoelastic relaxation detectable with GNSS networks, even at a large distance from the fault.

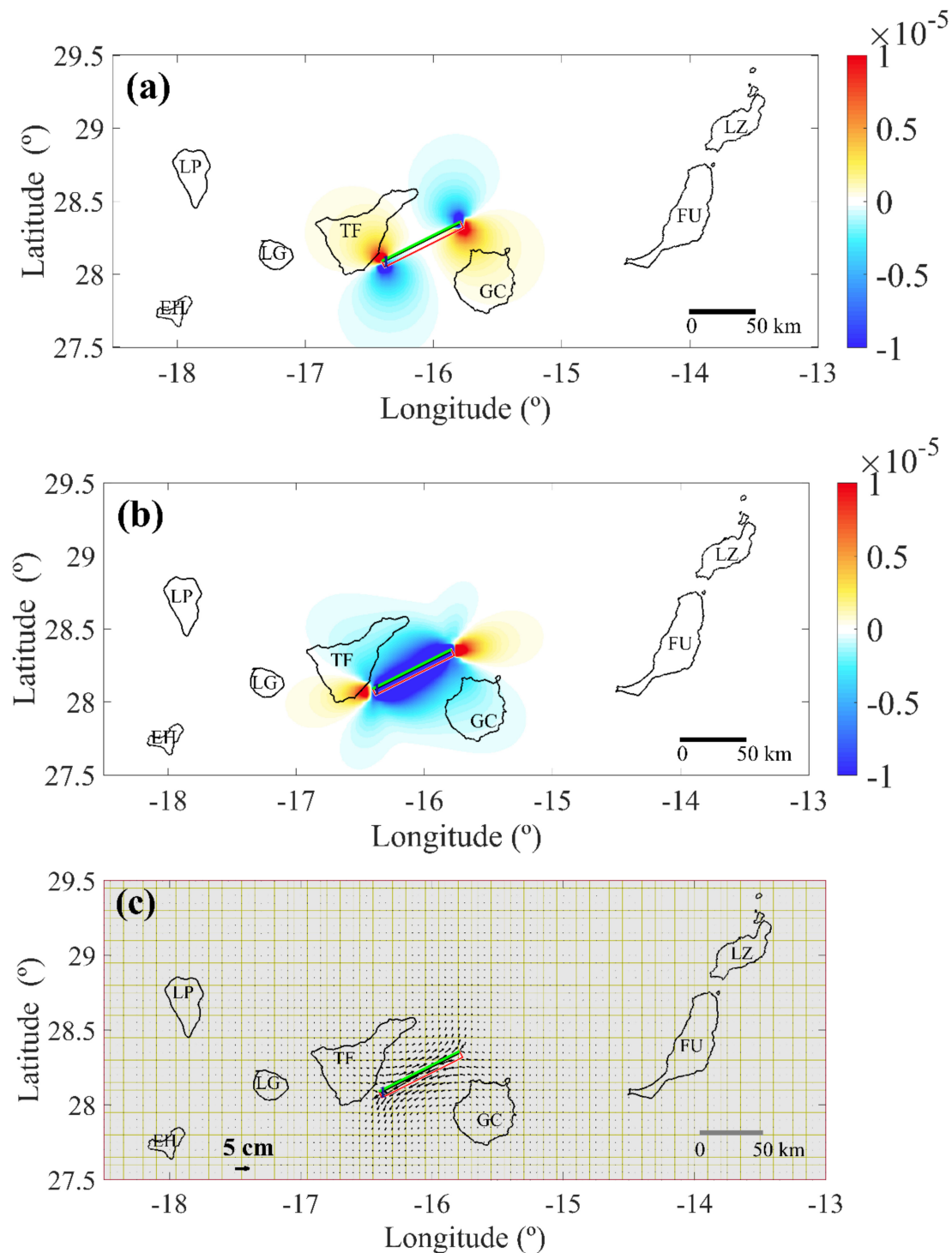


Figure 6. Dilatation (a), shear strain (b) and horizontal displacement (c) computed with Coulomb 3.4 software using the focal mechanisms of the 1989 earthquake (m_{bLg} 5.2, depth 15 km, strike 33° , dip 71° , slip 166°). The top and bottom depths of the active fault are set to 0 and 15 km, respectively, and the calculation depth is set to 4 km. The green line is the fault trace at the surface, while the red line is the projection to the surface of the fault frame; the black line is where the fault intersects the depth (the fault line at the target depth: 4 km). The blue digit refers to the number of dislocation sources used in the calculation.

Table 5. Summary of the Coulomb 3.4 modelling parameters used in the computation for the 1989 earthquake (m_{bLg} 5.2) displayed in Figure 6.

Parameter	
Poisson's ratio	0.25
Young modulus	80.0 GPa
Friction coefficient	0.4
Fault length	15.0 km
Calculation depth	4.0 km

The map of maximum shear strain (Figure 5) displays large shear onshore and offshore Gran Canaria in NE–SW orientation, accounting for a strain of 130×10^{-9} , with increasing strain generally from North to South. Such a pattern seems to be influenced by the regional stress field (e.g., [32]). The seismicity in that strip is concentrated offshore, on the one hand to the west, very near the seismic swarm related to the submarine fault. On the other hand, seismicity near the east coast of Gran Canaria appears even more scattered, preferentially distributed along the volcano-tectonic line described by [28]. Other areas within the squared zone of Figure 5 exhibit a considerable reduction in the maximum shear strain.

The findings for Tenerife are particularly interesting because the areas of maximum shear strain correlate well with the areas of localized strain (see Figure 4a). The central area of Tenerife mainly includes the volcanic edifice called Las Cañadas, whose upper part is a caldera structure. Las Cañadas was formed as a result of intense explosive volcanic activity, with the Teide-Pico Viejo (TPV) twin stratovolcanoes in the northern sector of the caldera [66–69]. TPV is one of the highest volcanic complexes on Earth (7200 m from the seafloor) and worthy of study due to its proximity to densely populated areas and proneness to future eruptions. TPV suffered an episode of unrest during 2004–2005, which was interpreted as deep magma injection beneath the volcano in the northwest area that later migrated to the southeast flank. Although no significant ground deformation has been reported, the observed gravity changes correlate well with seismicity [59,60,70,71]. Ref. [72], after reviewing the seismic database from the Spanish National Geographic Institute (<http://www.ign.es>) from 2003 to 2016, reported that except for the reawakening of 2004–2005 and the isolated seismic swarm of October 2016, the seismicity in Tenerife remained within the background levels. According to Figure 5, a relative maximum of shear strain appears in the central-western area of Tenerife, and another high of greater magnitude (up to 160×10^{-9}) is located to the northeast of the island. The relatively high values of shear strain situated in the central–western zone form an elongated area with an E–W orientation, with a cluster of epicentres concentrated along its orthogonal direction. This higher strain area encompasses a high-density crustal structure detected by [73,74] in the southwestern part of the Las Cañadas caldera, which produces a high residual gravity anomaly linked with the Boca Tauce central volcanic edifice. The area between these two highs of shear strain along Tenerife defines a fringe with a slight reduction in shear strain trending NW–SE (approximately 100×10^{-9}). This fringe overlaps an important number of epicentres situated in the Dorsal (NE) rift slope and along the Güimar valley. This area is affected by important tectonic activity, and the SE part of this area could be linked to the movements of the active faults situated between the islands of Tenerife and Gran Canaria. Indeed, the authors of [12] have already detected the presence of horizontal ground displacements along this NW–SE axis. In the context of the geodynamics of Tenerife, the SE sector is acknowledged to be an area of intense tectonic activity and anomalous kinematics. The kinematic behaviour of the NW sector of this NW–SE axis was already associated with volcanic activity during the 2004–2005 crisis. In light of the strain regime retrieved from GPS data, the location of the epicentres, the low-density materials and the low P-wave velocities found in that zone [73–75]. Ref. [16] proposed a geodynamic scheme that confirms NW Tenerife as more susceptible to volcanic activity than surrounding areas.

The higher values of shear strain in central west Tenerife continue offshore, connecting with another high situated to the north of La Gomera Island, also with an E–W orientation (Figure 5).

The epicentres follow the volcano-tectonic line reported by [28] that crosses Tenerife and La Gomera at the areas of maximum shear strain, mostly to the north of Tenerife, although seismicity rarely occurs to the northeast of La Gomera.

The high shear strain area with an elongated form is remarkable, and the E–W orientation is observed northeast of Tenerife, extending inland and offshore on both sides of the coast. There are also epicentres falling within this high shear strain area, mostly offshore. Many of these epicentres follow the NW–SE line crossing the island that is coincident with volcanic seamounts and the volcano-tectonic lineation reported by [25]. This line continues west of Gran Canaria, where other high shear strain appears. Indeed, this last high occupies most of the island territory and extends offshore (to the East) with an E–W orientation. The lower limits of the contour map we produced prevent a clearer definition of this high shear strain area that could continue to the south of Gran Canaria. However, the seismicity reported during the period of analysis is located in the area of high shear strain situated to the East, offshore of Gran Canaria, and follows another volcano-tectonic line oriented in the NE–SW orientation proposed by [28].

The analysis and modelling of aeromagnetic anomalies in Tenerife [38] and La Gomera [40] revealed that E–W tectonic features controlled the emplacement of magmas during the early formation of these islands since the most important intrusive complexes formed at the initial stages of their volcanic history are elongated in that direction. This implies that the E–W tectonic lineaments inferred from the present GNSS study represent long-lived tectonic features that have been active during the entire history of the Canary archipelago, from the Miocene to the present. This statement can also be extended to tectonic features with orientations from NE–SW to ENE–WSW between Tenerife and Gran Canaria, first suggested by [28] and later confirmed by other geophysical studies (e.g., [33,39]) and the present work.

6. Conclusions

From approximately 7 years of GNSS daily solutions (between 2011 and 2017), we reconstructed the present-day pattern of the active deformation in the Canary Archipelago through strain mapping. The 2D infinitesimal strain field was retrieved by computing high-precision geodetic horizontal velocities for 18 GNSS permanent stations, spanning the Canary Islands, and applying the triangular segmentation approach. This has enabled us to characterize major regions of deformation along the archipelago. The extension pattern along the archipelago is clear, with the sectors of maximum deformation found west of Tenerife, Gran Canaria and Fuerteventura. The analysis of the maximum shear strain mostly suggests E–W and NE–SW orientation patterns, suggesting that the regional stress field likely influences such orientations. The sharp change in shear strain between Tenerife and Gran Canaria identifies a sector of intense seismicity, which is mostly associated with the major submarine fault that separates the two insular edifices. On this submarine main tectonic structure, we have produced a tentative simulation of the horizontal deformation and strain caused by one of the strongest (m_{bLg} 5.2) earthquakes of the region. The retrieved dilatation, maximum shear strain and displacement agree with the strain field determined from the GNSS data. In addition, the inferred submarine alignment that crosses Tenerife in the NW–SE direction also concentrates offshore seismicity, which is distributed along areas of higher shear strain elongated in the E–W direction.

We observe a varying kinematic behaviour within the islands, with the Tenerife area being the most active with regard to the regional geodynamics of the entire archipelago. The absence of eruptive activity during the period analysed in this work, except for the El Hierro submarine eruption (October 2011–March 2012) (e.g., [70]), which falls outside the calculated strain maps drawn in this study, the seismic areas between islands, mainly offshore Tenerife and Gran Canaria, seem predominantly influenced by regional tectonic stress rather than by volcanic activity. As suggested by [39], the different episodes of volcanism in the Canary Islands could have occurred in a framework of both extensional and compressional tectonic regimes, and our present results seem to confirm this hypothesis.

Finally, the present work might be useful to improve hazard warnings in active volcanic areas, such as the Canary Islands region; certainly, GNSS networks must be an inherent part of earthquake and/or volcanic eruption warning systems. However, more geophysical and geodetic data of the Canary Archipelago are necessary for producing a complete map of its kinematics and tectonics.

Supplementary Materials: The following are available online at <http://www.mdpi.com/2072-4292/12/20/3297/s1>. The material shows the configuration of the 23 triangles formed for each triplet of GNSS stations. Figure S1: Triangles formed from 3 non-co-linear stations each, for the 23 GNSS stations used in this work (see Table 1). The horizontal strain was subsequently calculated for each triangle's centroid.

Author Contributions: Conceptualization, J.A., U.R. and M.B.; methodology, J.A., U.R., U.T. and M.B.; software, U.R., U.T. and J.A.; writing—original draft preparation, J.A. and U.R.; writing—review and editing, J.A., U.R., U.T., M.B., F.G.M., I.B.-M. and E.V.; visualization, J.A.; funding acquisition, J.A. All authors have read and agreed to the published version of the manuscript.

Funding: Project CGL2015-63799-P of the Spanish Research Agency has supported this research.

Acknowledgments: We wish to acknowledge MAGNET database [6] for providing us with GNSS data. The authors are grateful to two anonymous Reviewers and the Academic Editor for their positive and constructive comments.

Conflicts of Interest: The authors declare no conflict of interest.

References

1. Chousianitis, K.; Ganas, A.; Evangelidis, C.P. Strain and rotation rate patterns of mainland Greece from continuous GPS data and comparison between seismic and geodetic moment release. *J. Geophys. Res. Solid Earth* **2015**, *120*, 3909–3931. [[CrossRef](#)]
2. Savage, J.C. Euler-Vector Clustering of GPS Velocities Defines Microplate Geometry in Southwest Japan. *J. Geophys. Res. Solid Earth* **2018**, *123*, 1954–1968. [[CrossRef](#)]
3. Tzanas, A.; Chailas, S.; Sakkas, V.; Lagios, E. Tectonic deformation in the Santorini volcanic complex (Greece) as inferred by joint analysis of gravity, magnetotelluric and DGPS observations. *Geophys. J. Int.* **2019**, *220*, 461–489. [[CrossRef](#)]
4. Haines, A.J.; Wallace, L.M. New Zealand-Wide Geodetic Strain Rates Using a Physics-Based Approach. *Geophys. Res. Lett.* **2020**, *47*, e2019GL084606. [[CrossRef](#)]
5. Bastos, L.; Bos, M.S.; Fernandes, R.M. Deformation and Tectonics: Contribution of GPS Measurements to Plate Tectonics—Overview and Recent Developments. In *Sciences of Geodesy-I*; Xu, G., Ed.; Springer: Berlin/Heidelberg, Germany, 2010; pp. 155–184. [[CrossRef](#)]
6. Blewitt, G.; Hammond, W.C.; Kreemer, C. Harnessing the GPS Data Explosion for Interdisciplinary Science. *Eos* **2018**, *99*, 99. [[CrossRef](#)]
7. Larson, K.M. Unanticipated Uses of the Global Positioning System. *Annu. Rev. Earth Planet. Sci.* **2019**, *47*, 19–40. [[CrossRef](#)]
8. Wdowinski, S.; Bock, Y.; Zhang, J.; Fang, P.; Genrich, J. Southern California permanent GPS geodetic array: Spatial filtering of daily positions for estimating coseismic and postseismic displacements induced by the 1992 Landers earthquake. *J. Geophys. Res. Space Phys.* **1997**, *102*, 18057–18070. [[CrossRef](#)]
9. Martín, A.; Sevilla, M.; Zurutuza, J. Crustal deformation study in the Canary Archipelago by the analysis of GPS observations. *J. Appl. Geodesy* **2014**, *8*, 129–140. [[CrossRef](#)]
10. López, C.; García-Cañada, L.; Martí, J.; Cerdeña, I.D. Early signs of geodynamic activity before the 2011–2012 El Hierro eruption. *J. Geodyn.* **2017**, *104*, 1–14. [[CrossRef](#)]
11. Fernández, J.; Yu, T.-T.; Rodríguez-Velasco, G.; González-Matesanz, J.; Romero, R.; Rodríguez, G.; Quiros, R.; Dalda, A.; Aparicio, A.; Blanco, M. New geodetic monitoring system in the volcanic island of Tenerife, Canary Islands, Spain. Combination of InSAR and GPS techniques. *J. Volcanol. Geotherm. Res.* **2003**, *124*, 241–253. [[CrossRef](#)]
12. Berrocoso, M.; Carmona, J.; Fernandez-Ros, A.; Perez-Pena, A.; Ortiz, R.; García, A. Kinematic model for Tenerife Island (Canary Islands, Spain): Geodynamic interpretation in the Nubian plate context. *J. Afr. Earth Sci.* **2010**, *58*, 721–733. [[CrossRef](#)]
13. García, A.; Fernández-Ros, A.; Berrocoso, M.; Marrero, J.M.; Prates, G.; De La Cruz-Reyna, S.; Ortiz, R. Magma displacements under insular volcanic fields, applications to eruption forecasting: El Hierro, Canary Islands, 2011–2013. *Geophys. J. Int.* **2014**, *197*, 322–334. [[CrossRef](#)]

14. Riccardi, U.; Arnoso, J.; Benavent, M.; Velez, E.; Tammaro, U.; Montesinos, F.G. Exploring deformation scenarios in Timanfaya volcanic area (Lanzarote, Canary Islands) from GNSS and ground based geodetic observations. *J. Volcanol. Geotherm. Res.* **2018**, *357*, 14–24. [[CrossRef](#)]
15. Barbero, I.; Torrecillas, C.; Prates, G.; Páez, R.; Garate, J.; García, A.; Berrocoso, M. Assessment of ground deformation following Tenerife's 2004 volcanic unrest (Canary Islands). *J. Geodyn.* **2018**, *121*, 1–8. [[CrossRef](#)]
16. Alzola, A.S.; Martí, J.; García-Yeguas, A.; Gil, A.J. Subsidence and current strain patterns on Tenerife Island (Canary Archipelago, Spain) derived from continuous GNSS time series (2008–2015). *J. Volcanol. Geotherm. Res.* **2016**, *327*, 240–248. [[CrossRef](#)]
17. Ancochea, E.; Brändle, J.; Cubas, C.; Hernan, F.; Huertas, M. Volcanic complexes in the eastern ridge of the Canary Islands: the Miocene activity of the island of Fuerteventura. *J. Volcanol. Geotherm. Res.* **1996**, *70*, 183–204. [[CrossRef](#)]
18. Carracedo, J.C.; Pérez Torrado, F.J.; Ancochea, E.; Meco, J.; Hernán, F.; Cubas, C.R.; Casillas, R.; Rodríguez Badiola, E.; Ahijado, A. Cenozoic volcanism II: The Canary Islands. In *The Geology of Spain*; Gibbons, W., Moreno, T., Eds.; Geological Society London: London, UK, 2002; p. 632.
19. Watts, A.B.; Peirce, C.; Collier, J.S.; Dalwood, R.; Canales, J.P.; Henstock, T.J. A seismic study of lithospheric flexure in the vicinity of Tenerife, Canary Islands. *Earth Planet. Sci. Lett.* **1997**, *146*, 431–447. [[CrossRef](#)]
20. Schmincke, H.U. *Volcanism*; Springer: Berlin/Heidelberg, Germany, 2004; p. 324. [[CrossRef](#)]
21. Llanes, P. Estructura de la Litosfera en el Entorno de las Islas Canarias a Partir del Análisis Gravimétrico e Isostático: Implicaciones Geodinámicas. Ph.D. Thesis, Univ. Complutense of Madrid, Madrid, Spain, 2006; p. 195.
22. Troll, V.R.; Carracedo, J.C. *The Geology of the Canary Islands*; Elsevier BV: Amsterdam, The Netherlands, 2016; p. 636.
23. Carracedo, J.C. Growth, structure, instability and collapse of Canarian volcanoes and comparisons with Hawaiian volcanoes. *J. Volcanol. Geotherm. Res.* **1999**, *94*, 1–19. [[CrossRef](#)]
24. Mantovani, E.; Viti, M.; Babbucci, D.; Albarello, D. Nubia-Eurasia kinematics: An alternative interpretation from Mediterranean and North Atlantic evidence. *Ann Geophys.* **2007**, *50*, 341–366. [[CrossRef](#)]
25. Ruiz, C.; García-Cacho, L.; Arana, V.; Luque, A.; Felpeto, A. Submarine volcanism surrounding Tenerife, Canary Islands: Implications for tectonic controls, and oceanic shield forming processes. *J. Volcanol. Geotherm. Res.* **2000**, *103*, 105–119. [[CrossRef](#)]
26. Anguita, F.; Hernan, F. The Canary Islands origin: A unifying model. *J. Volcanol. Geotherm. Res.* **2000**, *103*, 1–26. [[CrossRef](#)]
27. Anguita, F.; Hernan, F. A propagating fracture model versus a hot spot origin for the Canary islands. *Earth Planet. Sci. Lett.* **1975**, *27*, 11–19. [[CrossRef](#)]
28. Bosshard, E.; Macfarlane, D.J. Crustal structure of the western Canary Islands from seismic refraction and gravity data. *J. Geophys. Res. Space Phys.* **1970**, *75*, 4901–4918. [[CrossRef](#)]
29. Zhao, D.; Lei, J.; Inoue, T.; Yamada, A.; Gao, S.S. Deep structure and origin of the Baikal rift zone. *Earth Planet. Sci. Lett.* **2006**, *243*, 681–691. [[CrossRef](#)]
30. Fourel, L.; Milelli, L.; Jaupart, C.; Limare, A. Generation of continental rifts, basins, and swells by lithosphere instabilities. *J. Geophys. Res. Solid Earth* **2013**, *118*, 3080–3100. [[CrossRef](#)]
31. Duggen, S.; Hoernle, K.; Hauff, F.; Kluegel, A.; Bouabdellah, M.; Thirlwall, M.F. Flow of Canary mantle Plume material through a subcontinental lithospheric corridor beneath Africa to the Mediterranean: REPLY. *Geology* **2010**, *38*, e203. [[CrossRef](#)]
32. Geyer, A.; Marti, J.; Villaseñor, A. First-order estimate of the Canary Islands plate-scale stress field: Implications for volcanic hazard assessment. *Tectonophysics* **2016**, *679*, 125–139. [[CrossRef](#)]
33. Mezcua, J.; Buforn, E.; Udias, A.; Rueda, J. Seismotectonics of the Canary Islands. *Tectonophysics* **1992**, *208*, 447–452. [[CrossRef](#)]
34. Del Fresno, C.; Cerdeña, I.D.; Cesca, S.; Buforn, E. The 8 October 2011 Earthquake at El Hierro (Mw 4.0): Focal Mechanisms of the Mainshock and Its Foreshocks. *Bull. Seism. Soc. Am.* **2014**, *105*, 330–340. [[CrossRef](#)]
35. Telesca, L.; Lovallo, M.; López, C.; Molist, J.M. Multiparametric statistical investigation of seismicity occurred at El Hierro (Canary Islands) from 2011 to 2014. *Tectonophysics* **2016**, *672*, 121–128. [[CrossRef](#)]
36. Jiménez-Munt, I.; Fernández, M.; Torne, M.; Bird, P.; Torne, M. The transition from linear to diffuse plate boundary in the Azores–Gibraltar region: Results from a thin-sheet model. *Earth Planet. Sci. Lett.* **2001**, *192*, 175–189. [[CrossRef](#)]

37. Jiménez-Munt, I.; Negrodo, A.M. Neotectonic modelling of the western part of the Africa–Eurasia plate boundary: From the Mid-Atlantic ridge to Algeria. *Earth Planet. Sci. Lett.* **2003**, *205*, 257–271. [[CrossRef](#)]
38. Blanco-Montenegro, I.; Nicolosi, I.; Pignatelli, A.; García, A.; Chiappini, M. New evidence about the structure and growth of ocean island volcanoes from aeromagnetic data: The case of Tenerife, Canary Islands. *J. Geophys. Res. Space Phys.* **2011**, *116*. [[CrossRef](#)]
39. Blanco-Montenegro, I.; Montesinos, F.G.; Arnosó, J. Aeromagnetic anomalies reveal the link between magmatism and tectonics during the early formation of the Canary Islands. *Sci. Rep.* **2018**, *8*, 42. [[CrossRef](#)]
40. Blanco-Montenegro, I.; Montesinos, F.G.; Nicolosi, I.; Arnosó, J.; Chiappini, M. Three-Dimensional Magnetic Models of La Gomera (Canary Islands): Insights Into the Early Evolution of an Ocean Island Volcano. *Geochem. Geophys. Geosystems* **2020**, *21*, 2019gc008787. [[CrossRef](#)]
41. Kreemer, C.; Blewitt, G.; Klein, E.C. A geodetic plate motion and Global Strain Rate Model. *Geochem. Geophys. Geosyst.* **2014**, *15*, 3849–3889. [[CrossRef](#)]
42. Moritz, H. *Advanced Least-Square Methods. Reports of the Department of Geodetic Science; Report 175*; Ohio State University: Columbus, OH, USA, 1972; p. 129.
43. Allmendinger, R.W.; Cardozo, N.; Fisher, D.M. *Structural Geology Algorithms*; Cambridge University Press (CUP): Cambridge, UK, 2011.
44. Shen, Z.-K.; Jackson, D.D.; Ge, B.X. Crustal deformation across and beyond the Los Angeles basin from geodetic measurements. *J. Geophys. Res. Space Phys.* **1996**, *101*, 27957–27980. [[CrossRef](#)]
45. Wu, Y.; Jiang, Z.-S.; Yang, G.; Wei, W.; Liu, X. Comparison of GPS strain rate computing methods and their reliability. *Geophys. J. Int.* **2011**, *185*, 703–717. [[CrossRef](#)]
46. Szafarczyk, A.; Ulmaniec, M.; Borowiec, W. An attempt to apply tensor calculus to evaluate the deformation condition of vertical upper embankment zones for a landfill located in a mining area, based on satellite measurement results. *Rep. Geod.* **2007**, *82*, 317–326.
47. Tammaro, U.; DeMartino, P.; Obrizzo, F.; Brandi, G.; D’Alessandro, A.; Dolce, M.; Malaspina, S.; Serio, C.; Pingue, F. Somma Vesuvius volcano: Ground deformations from CGPS observations (2001–2012). *Ann. Geophys.* **2013**, *56*, S0456. [[CrossRef](#)]
48. Araszkiwicz, A. Reference Frame Realization Impact on Network Deformation—Geodynamic Research in Tectonic Stable Areas. In Proceedings of the 14th SGEM GeoConference on Informatics, Geoinformatics and Remote Sensing, Albena, Bulgaria, 17–26 June 2014; STEF92 Technology Ltd.: Sofia, Bulgaria, 2014; Volume 2, pp. 427–434.
49. Segall, P. *Earthquake and Volcano Deformation*; Walter de Gruyter GmbH: Berlin, Germany, 2010; p. 432.
50. Luzum, B.; Petit, G. The IERS Conventions (2010): Reference systems and new models. *Proc. Int. Astron. Union* **2012**, *10*, 227–228. [[CrossRef](#)]
51. Lyard, F.; Lefevre, F.; Letellier, T.; Francis, O. Modelling the global ocean tides: Modern insights from FES2004. *Ocean. Dyn.* **2006**, *56*, 394–415. [[CrossRef](#)]
52. Altamimi, Z.; Rebischung, P.; Métivier, L.; Collilieux, X. ITRF2014: A new release of the International Terrestrial Reference Frame modeling nonlinear station motions. *J. Geophys. Res. Solid Earth* **2016**, *121*, 6109–6131. [[CrossRef](#)]
53. Jaeger, J.C.; Cook, N.G.W.; Zimmerman, R.W. *Fundamentals of Rock Mechanics*, 4th ed.; Blackwell Publishing Ltd.: Hoboken, NJ, USA, 2007; ISBN 13: 978-0-632-05759-7.
54. DeMets, C.; Gordon, R.G.; Vogt, P. Location of the Africa–Australia–India Triple Junction and Motion between the Australian and Indian Plates: Results from an Aeromagnetic Investigation of the Central Indian and Carlsberg Ridges. *Geophys. J. Int.* **1994**, *119*, 893–930. [[CrossRef](#)]
55. González, P.J.; Fernández, J. Error estimation in multitemporal InSAR deformation time series, with application to Lanzarote, Canary Islands. *J. Geophys. Res. Space Phys.* **2011**, *116*. [[CrossRef](#)]
56. Ancochea, E.; Fuster, J.; Ibarrola, E.; Cendrero, A.; Coello, J.; Hernan, F.; Cantagrel, J.M.; Jamond, C. Volcanic evolution of the island of Tenerife (Canary Islands) in the light of new K–Ar data. *J. Volcanol. Geotherm. Res.* **1990**, *44*, 231–249. [[CrossRef](#)]
57. Fernández, J.; Tizzani, P.; Manzo, M.; Borgia, A.; González, P.J.; Martí, J.; Pepe, A.; Camacho, A.G.; Casu, F.; Berardino, P.; et al. Gravity-driven deformation of Tenerife measured by InSAR time series analysis. *Geophys. Res. Lett.* **2009**, *36*, 04306. [[CrossRef](#)]
58. De Vallejo, L.I.G.; García-Mayordomo, J.; Insua-Arévalo, J.M. Probabilistic Seismic-Hazard Assessment of the Canary Islands. *Bull. Seism. Soc. Am.* **2006**, *96*, 2040–2049. [[CrossRef](#)]

59. García, A.; Ortiz, R.; Marrero, J.M.; Sánchez, N.; Vila, J.; Correig, A.M.; Marcià, R.; Sleeman, R.; Tárraga, M. Monitoring the reawakening of Canary Islands' Teide Volcano. *Eos* **2006**, *87*, 61. [[CrossRef](#)]
60. Gottsmann, J.; Wooller, L.; Marti, J.; Fernandez, J.; Camacho, A.G.; González, P.J.; García, A.; Rymer, H. New evidence for the reawakening of Teide volcano. *Geophys. Res. Lett.* **2006**, *33*, 20311. [[CrossRef](#)]
61. Fernández, C.; De La Nuez, J.; Casillas, R.; García-Navarro, E. Stress fields associated with the growth of a large shield volcano (La Palma, Canary Islands). *Tectonics* **2002**, *21*, 13-1–13-18. [[CrossRef](#)]
62. Toda, S.; Stein, R.S.; Richards-Dinger, K.; Bozkurt, S.B. Forecasting the evolution of seismicity in southern California: Animations built on earthquake stress transfer. *J. Geophys. Res. Space Phys.* **2005**, *110*. [[CrossRef](#)]
63. Lin, J.; Stein, R.S. Stress triggering in thrust and subduction earthquakes and stress interaction between the southern San Andreas and nearby thrust and strike-slip faults. *J. Geophys. Res. Space Phys.* **2004**, *109*. [[CrossRef](#)]
64. Okada, Y. Internal deformation due to shear and tensile faults in a half-space. *Bull. Seismol. Soc. Am.* **1992**, *82*, 1018–1040.
65. Hearn, E.H. What can GPS data tell us about the dynamics of post-seismic deformation? *Geophys. J. Int.* **2003**, *155*, 753–777. [[CrossRef](#)]
66. Ablay, G.J.; Palmer, M.R.; Carroll, M.; Marti, J.; Sparks, R.S.J. Basanite-Phonolite Lineages of the Teide-Pico Viejo Volcanic Complex, Tenerife, Canary Islands. *J. Pet.* **1998**, *39*, 905–936. [[CrossRef](#)]
67. Ancochea, E.; Huertas, M.; Cantagrel, J.; Coello, J.; Fúster, J.; Arnaud, N.; Ibarrola, E. Evolution of the Cañadas edifice and its implications for the origin of the Cañadas Caldera (Tenerife, Canary Islands). *J. Volcanol. Geotherm. Res.* **1999**, *88*, 177–199. [[CrossRef](#)]
68. Carracedo, J.C.; Badiola, E.R.; Guillou, H.; Paterne, M.; Scaillet, S.; Perez-Torrado, F.J.; Paris, R.; Fra-Paleo, U.; Hansen, A. Eruptive and structural history of Teide Volcano and rift zones of Tenerife, Canary Islands. *GSA Bull.* **2007**, *119*, 1027–1051. [[CrossRef](#)]
69. Marti, J.; Geyer, A.; Andújar, J.; Teixidó, F.; Costa, F. Assessing the potential for future explosive activity from Teide–Pico Viejo stratovolcanoes (Tenerife, Canary Islands). *J. Volcanol. Geotherm. Res.* **2008**, *178*, 529–542. [[CrossRef](#)]
70. Almendros, J.; Ibáñez, J.; Carmona, E.; Zandomenighi, D. Array analyses of volcanic earthquakes and tremor recorded at Las Cañadas caldera (Tenerife Island, Spain) during the 2004 seismic activation of Teide volcano. *J. Volcanol. Geotherm. Res.* **2007**, *160*, 285–299. [[CrossRef](#)]
71. Marti, J.; Ortiz, R.; Gottsmann, J.; García, A.; De La Cruz-Reyna, S. Characterising unrest during the reawakening of the central volcanic complex on Tenerife, Canary Islands, 2004–2005, and implications for assessing hazards and risk mitigation. *J. Volcanol. Geotherm. Res.* **2009**, *182*, 23–33. [[CrossRef](#)]
72. Cerdeña, I.D.; Del Fresno, C.; Cantavella, J.V.; Felpeto, A.; Lozano, L.; Medina, L.C.; Torres, P.A.; Luengo-Oroz, N.; Solares, J.M.M.; Blanco, M.; et al. Comment on “Geochemical evidences of seismo-volcanic unrests at the NW rift-zone of Tenerife, Canary Islands, inferred from diffuse CO₂ emission” by Hernández P. A., Padilla G., Barrancos J., Melián G., Padrón E., Asensio-Ramos M., Rodríguez F., Pérez N. M., Alonso M., and Calvo D. [*Bull. Volcanol.* (2017) 79:30]. *Bull. Volcanol.* **2017**, *80*, 1–4. [[CrossRef](#)]
73. Gottsmann, J.; Camacho, A.G.; Marti, J.; Wooller, L.; Fernandez, J.; García, A.; Rymer, H. Shallow structure beneath the Central Volcanic Complex of Tenerife from new gravity data: Implications for its evolution and recent reactivation. *Phys. Earth Planet. Inter.* **2008**, *168*, 212–230. [[CrossRef](#)]
74. Aparicio, S.S.-M.; Martí, J.; Montesinos, F.; Gómez, A.B.; De Pablo, J.P.; Fernández, P.V.; García-Maroto, M.C. Gravimetric study of the shallow basaltic plumbing system of Tenerife, Canary Islands. *Phys. Earth Planet. Inter.* **2019**, *297*, 106319. [[CrossRef](#)]
75. Garcia-Yeguas, A.; Koulakov, I.; Ibáñez, J.; Rietbrock, A. High resolution 3D P wave velocity structure beneath Tenerife Island (Canary Islands, Spain) based on tomographic inversion of active-source data. *J. Geophys. Res. Space Phys.* **2012**, *117*, 09309. [[CrossRef](#)]

